RSC Advances

ROYAL SOCIETY OF CHEMISTRY

www.rsc.org/advances

Journal Name

ARTICLE

Effect of carbon contents and electronic strong correlation on mechanical and thermodynamic properties of ytterbium carbides

Received 00th January 20xx,
Accepted 00th January 20xx

DOI: 10.1039/x0xx00000x

www.rsc.org/

Wei Dong[a], Chao Zhang[a†], Hong Jiang[a], Yue-Hua Su[a], and Zhen-Hong Dai[a]

The mechanical and thermodynamic properties of four ytterbium carbides with increasing carbon contents have been examined using *ab initio* calculations based on density functional theory. In order to describe the strong on-site Coulomb repulsion among localized 4*f* electrons, generalized gradient approximation plus a Hubbard parameter (GGA + *U*) formalisms have been adopted for the exchange correlation term. The elastic constants of YbC, Yb_2C_3, YbC_2, and YbC_6 are related to Hubbard *U*. The bulk modulus *B*, shear modulus *G*, and Young's modulus *E* are evaluated through Voigt-Reuss-Hill approximation. Among the four ytterbium carbides, YbC_6 yields the largest *B*, *G*, and *E*, and YbC_2 exhibits relatively soft and ductile characteristics. Mechanical anisotropy was estimated using several anisotropic indexes and factors. The anisotropic property of *E* of four ytterbium carbides is more evident than that of *B*. Phonon calculation reveals the thermodynamic stability of YbC_2 and YbC_6, which is consistent with experimental observations.

1. Introduction

Metal carbides have been extensively investigated from both experimental and theoretical points of view because of their unique magnetic and electrical properties for electronic applications.[1-4] Rare-earth carbides has been commonly used as model systems to probe structure–property relationships because of their structural diversity. C atoms play a principal role in the structural diversity of rare-earth carbides. The C-to-metal atomic ratio in rare-earth carbides exhibits a broad range, for instance, the C-to-metal atomic ratios of CeC and EuC_6 are 1 and 6, respectively.[5-7] The C atoms in rare-earth carbides also exist in various forms, such as three-dimensional networks, two-dimensional layered structures, and C-C dumbbell units. Two-dimensional C layers are implicated in superconducting graphite intercalation compounds (GICs). The combination of the graphene and intercalated sheets is accounted for superconductivity because neither graphite nor pure metal exhibits a high T_c.[8] It is reported that the C–C dumbbell distance is correlated with T_c of rare-earth carbides superconductors.[9] The C–C distance in the C_2 dumbbell at approximately 1.30 Å shows the highest T_c among rare-earth carbides. The C_2 dumbbell is also found in $RE_xT_yC_2$ carbides, where RE denotes a rare-earth metal and T denotes a transition metal. C_2 and T form a quasi-one-dimensional linear TC_4 unit embedded in matrix RE cations. It is found that the medium-frequency C_2 vibrations drive the high T_c in Sc_3CoC_4.[10] Furthermore, C_2 dumbbell dimer unit could transfer to two-dimensional graphite sheets under pressure, such as in Ca-C systems.[11-13]

The past decade has been seen intense efforts directed at studies of the structures and properties of ytterbium carbides. The ytterbium-carbon systems are significantly different from those of lightweight rare-earth carbide systems, which have well defined dicarbides, Pu_2C_3-type sequicarbides, and NaCl-type monocarbides.[14, 15] However, NaCl-type monocarbides with a stoichiometric ratio of 1:1 has yet to be determined in Yb−C systems. Yb_3C is characterized by a C-deficient NaCl-type structure.[14] Although Yb_2C_3 with a body-centered cubic Pu_2C_3-type structure can be prepared at high pressures, the thermodynamic stability of this compound under ambient conditions remains elusive.[16] Similar to lightweight rare-earth carbides, YbC_2 assumes a tetragonal CaC_2-type structure.[17] Surprisingly, the lattice parameters of YbC_2 are different from other rare-earth dicarbides. The lattice parameters of rare-earth carbides decrease regularly with increasing of atomic number of metal atoms, by contrast, the lattice parameters of YbC_2 lie between those of HoC_2 and ErC_2.[14] The interest of ytterbium carbides is in part fueled by the discovery of superconductivity in YbC_6 with T_c of 6.5 K.[18] Two mechanisms have been proposed to understand the superconductivity of GICs, including YbC_6. Csanyi *et al*. proposed an unconventional exciton or plasmon-mediated pairing mechanism.[19] Later, a conventional BCS phonon-mediated mechanism has also been suggested; in this mechanism, interlayer bands display a sufficiently strong coupling with both in-plane intercalant and out-of-plane graphite phonon modes to allow for a relatively high T_c.[20, 21]

4*f* electrons play a pivotal role in understanding the electronic and thermodynamic properties of rare-earth compounds; however, conventional density function theory (DFT), which uses conventional exchange-correlation potential, such as local density functional approximation (LDA) or

[a] *Department of Physics, Yantai University, Yantai, 264005, China.*
† Email address: phyczhang@ytu.edu.cn

generalized gradient approximation (GGA), has failed to describe the ground state properties of systems containing 4*f* electrons because of their strong on-site Coulomb repulsion. An effective modification of pure DFT which calls LDA/GGA + *U* (*U* is the Hubbard energy) scheme[22-24] can be used to obtain considerable improvement with respect to the LDA or GGA results. In fact, DFT + *U* calculations have been performed to explore the electronic properties of ytterbium compounds. Including localized 4*f* orbitals in the LDA + *U* method results in the downward rigid shift of the energy of the filled 4*f* bands in YbC_6.[25] The more recently studies of novel correlated topological insulator YbB_6 reveals that the 4*f* band moves to a higher energy and does not cross the 5*d* band when turning on the Hubbard parameter *U*; this findings is consistent with experimental data.[26]

Although numerous studies on the structural and electronic properties of individual ytterbium carbide have been performed, theoretical studies on ytterbium carbides, especially mechanical and thermodynamic properties with respect to carbon contents have been rarely conducted. In addition, the effects of electronic strong correlation on ytterbium carbides have been sparsely visited. In this work, four representative ytterbium carbides with increasing carbon contents (YbC, Yb_2C_3, YbC_2, and YbC_6) were selected to systematically exmine their mechanical and thermodynamic properties through *ab initio* GGA+ *U* calculations.

2. Computational methods

The *ab initio* calculations were performed within the framework of DFT as implemented in the Vienna Ab-initio Simulation Package (VASP).[27] The all-electron projector augmented wave (PAW)[28] pseudopotential for Yb and C from the VASP pseudopotential library were used. The electron wave function was expanded in plane waves up to a cutoff energy of 550 eV. The *k*-point meshes[29] in the full edge of the Brillouin zone (BZ) are sampled of 2π × 0.02 $Å^{-1}$. Iteration relaxation of atomic positions and cell volume was stopped when the forces generally acting on the atoms were found to be smaller than 0.01 eV/Å. With this criterion, the change in total energy between successive steps was less than 0.01 meV/cell. The exchange and correlation energy was assessed by GGA in the scheme of Perdew-Burke-Ernzerhof (PBE).[30] The strong on-site Coulomb repulsion among the localized Yb 4*f* electrons was described by the DFT + *U* method[22, 24] developed by Dudarev *et al*.[23] In this scheme, the total GGA energy functional is defined as:

$$E_{GGA+U} = E_{GGA} + \frac{U-J}{2}\sum_{\sigma}[\mathrm{Tr}\rho^{\sigma} - \mathrm{Tr}(\rho^{\sigma}\rho^{\sigma})],$$

where ρ^{σ} is the density matrix of *f* states with spin *σ*, *U* and *J* are the spherically averaged screened Coulomb energy and exchange energy, respectively. Since only the difference between *U* and *J* is significant, thus we will henceforth label them as one single parameter *U* for simplicity, In the subsequent calculations, the parameter *U* varies from 1 to 5, and *U* = 0 means turning off the Hubbard *U* term.

Phonon calculations were performed by supercell approach and finite displacement method.[31] From finite displacements, the Hellmann-Feynman atomic forces computed at the optimized supercell by VASP code were transferred to the PHONOPY code[32, 33] to construct the dynamical matrix. Diagonalization of the dynamical matrix gives phonon frequencies and their corresponding density of states. In the interpolation of the constants for calculating the phonon dispersion, $3\times3\times3$, $2\times2\times2$, $3\times3\times3$, and $2\times2\times1$ supercells with *k*-point mesh of 2π × 0.02 $Å^{-1}$ were used for YbC, Yb_2C_3, YbC_2 and YbC_6. respectively. Thermodynamic properties can be determined by phonon calculations using the quasiharmonic approximation (QHA).[33] The phonon contribution to the Helmholtz free energy *F* is given by:

$$F = \frac{1}{2}\sum_{q,v}\hbar\omega(q,v) + k_BT\sum_{q,v}\ln[1-\exp(-\hbar\omega(q,v)/k_BT)],$$

where $\omega(q, v)$ is the phonon frequency at wave vector *q* and band *v,* and *T* is the temperature. k_B and $\hbar$ are the Boltzmann constants and the reduced Planck constants, respectively. The heat C_V and S are given by

$$C_V = k_B\sum_{q,v}(\frac{\hbar\omega(q,v)}{k_BT})^2\frac{\exp(\hbar\omega/k_BT)}{[\exp(\hbar\omega/k_B)-1]^2}$$

and

$$S = -k_B\sum_{q,v}\ln[1-\exp(-\hbar\omega(q,v)/k_BT)] - \frac{1}{T}\sum_{q,v}\frac{\hbar\omega(q,v)}{\exp(\hbar\omega(q,v)/k_BT)-1}$$

respectively.

3. Results and discussion

3.1 Equilibrium structural properties

YbC with a stoichiometric ratio of 1:1 adopts an ordered cubic NaCl-type structure (space group *Fm*-3*m*), in which Yb atoms assume Na positions and C atoms occupy Cl positions, as

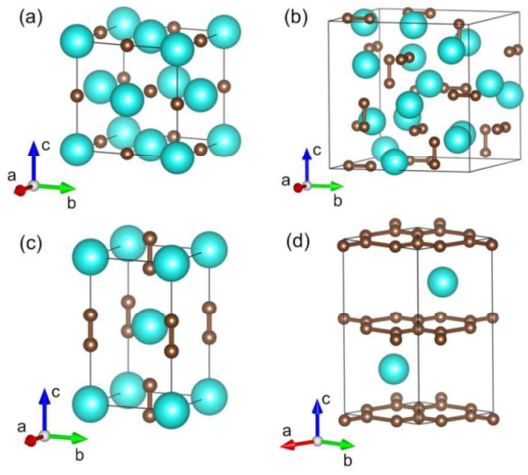

Fig. 1 Crystal structures of (a) YbC, (b) Yb_2C_3, (c) YbC_2, and (d) YbC_6. The large and small spheres represent Yb and C atoms, respectively.

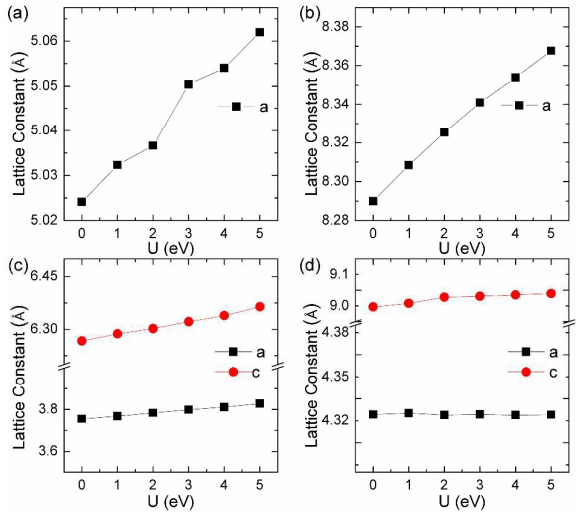

Fig. 2 Lattice constants as a function of Hubbard *U* for (a) YbC, (b) Yb_2C_3, (c)YbC_2, and (d) YbC_6.

shown in Fig. 1(a). The Yb atoms form a close-packed structure, whereas the C atoms enter octahedral interstices. The lattice constant *a* of YbC with various Hubbard *U* values are presented in Fig. 2(a). The lattice constants display a ladder shape as Hubbard *U* values increase. When Hubbard *U* is turned off, the calculated lattice constant *a* reaches 5.024 Å, which is the smallest value. At Hubbard *U* = 5 eV, the lattice constant *a* is 5.062 Å. Ytterbium sequicarbides, Yb_2C_3, assumes a cubic Pu_2C_3-type crystal structure (space group *I*-43*d*) with eight formula units (fu) in a conventional cell. The Yb atoms are aligned along the [111] direction, and the C atoms form dumbbell-shaped dimers occupying the voids in the bisphenoids of the Yb substructure. The calculated lattice constant *a* as a relationship of Hubbard *U* is shown in Fig. 2(b). The calculated lattice constant *a* of 8.290 Å at Hubbard *U* = 0 eV is 2.7% larger than the experimental value of 8.073Å.[16] Furthermore, the calculated C–C distances slightly decrease as Hubbard *U* value increases, from 1.314 Å at Hubbard *U* = 0 eV to 1.303 Å at Hubbard *U* = 5 eV. However, the difference between the calculated C–C distances with various Hubbard *U* values within 0.2% and the C–C dimer distances of Yb_2C_3 are close to the experimental value of 1.313 Å.[16]

YbC_2 crystallizes in a body-centered tetragonal CaC_2-type structure (space group *I4/mmm*), in which the C atoms exist in the form of a C–C dimer similar to that in Yb_2C_3. The C–C dimers oriented parallel to the *c* axis are six-fold coordinated by Yb atoms forming an elongated octahedron. As the Hubbard *U* increases from 0 eV to 5 eV, the lattice constants *a* and *c* increase by 1.9% and 1.6%, respectively. The calculated C–C dimer distances in YbC_2 with various Hubbard *U* remain almost unchanged and reach the experimental value of 1.293 Å.[17] Moreover, it is noteworthy that the C–C dimer distance in other Pu_2C_3- and CaC_2-type rare-earth carbides is approximately 1.3 Å, such as 1.298 Å in Y_2C_3,[34] 1.2942 Å in La_2C_3,[35] 1.2888 Å in YC_2,[36] and 1.303 Å in LaC_2.[37] This result indicates that the C–C dimer distance shows a weak dependence on the choice of metal atoms in these crystals.

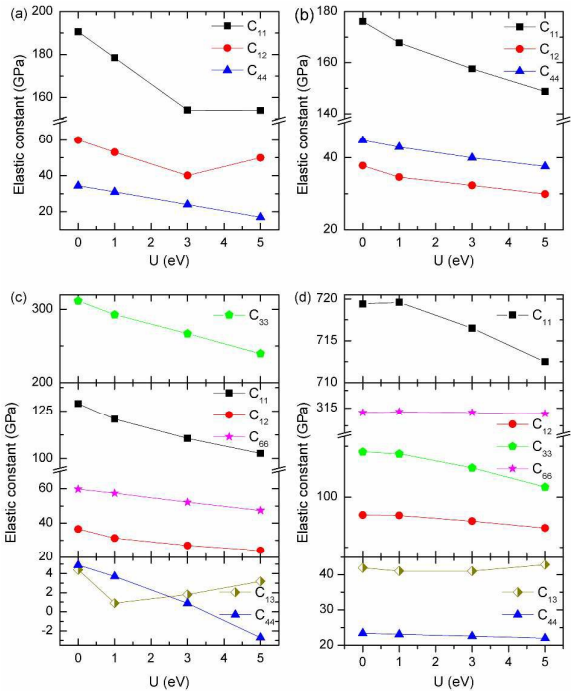

Fig. 3 Dependence of the elastic constants on Hubbard *U* for (a) YbC, (b) Yb_2C_3, (c) YbC_2, and (d) YbC_6.

Thus, it is not unexpected that the C-C dimer distances in Yb_2C_3 and YbC_2 change slightly with various Hubbard *U* because the Hubbard *U* correction is added on the 4*f* electrons of the Yb atoms. YbC_6, a famous kind of GICs, presents an *AαAβ* stacking where *A* corresponds to C layers and *α* and *β* represent the Yb intercalant layers. Interestingly, the lattice constant *c* significantly increases when Hubbard *U* increases; by contrast, the lattice constant *a* seems unaffected to Hubbard *U* and is approximately equals to 4.340 Å, which is close to the experimental value of 4.320 Å[6, 7] and the theoretical value of 4.340 Å.[38] In fact, the lattice parameters *a* slightly differs in other GICs, such as 4.29Å of NdC_6, and 4.314 Å of EuC_6.[6, 7]

3.2 Elastic constants and polycrystalline moduli

The elastic constants of a solid link the mechanical and dynamical behaviors and provide important information regarding the nature of the forces operating in the solids, such as stability and stiffness. The independent elastic constants of YbC, Yb_2C_3, YbC_2 and YbC_6 with various Hubbard *U* values are calculated from the strained structures, and the relationship between independent elastic constants and Hubbard *U* values is plotted in Fig. 3. There are three independent elastic constants for cubic YbC and Yb_2C_3, i.e., C_{11}, C_{12}, and C_{44}. The elastic constants of YbC and Yb_2C_3 decrease as Hubbard *U* increases except C_{12} of YbC. The elastic constant C_{12} of YbC first falls to 40.1 GPa at Hubbard *U* = 3 eV and then rises to 50 GPa at Hubbard *U* = 5 eV, forming a valley at Hubbard *U* = 3 eV, as shown in Fig. 3(a). For the relatively low-symmetry tetragonal YbC_2 and hexagonal YbC_6, there are six independent elastic constants. Similar to the elastic constants of YbC and Yb_2C_3 systems, most of the elastic constants of YbC_2 and YbC_6

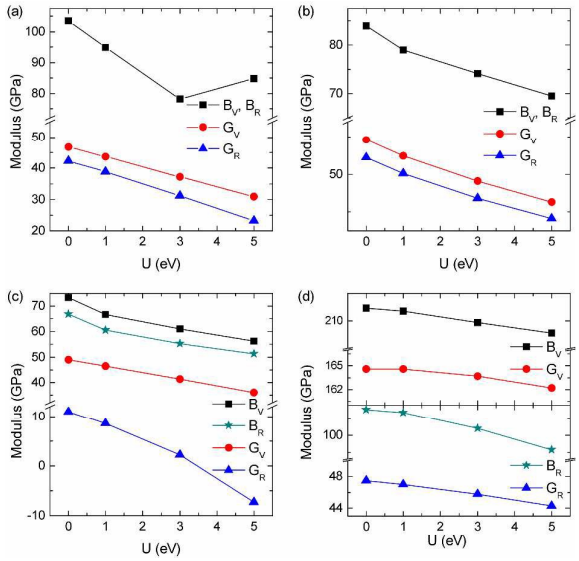

Fig. 4 Calculated bulk modulus *B* and shear modulus *G* of YbC, Yb_2C_3, YbC_2 and YbC_6 under Voigt and Reuss approximations with various Hubbard *U* values.

decrease when Hubbard *U* increases. The elastic constant C_{33} of YbC_2 and YbC_6 decreases by approximately 23% and 14% from Hubbard *U* = 0 eV to 5 eV, respectively. Interestingly, the elastic constant C_{13} of YbC_2 and YbC_6 initially decreases and then increases as Hubbard *U* increases. The elastic constant C_{11} of YbC_6 is the largest among the elastic constants of the four ytterbium carbides; in particular, C_{11} of YbC_6 is 719 GPa and 713 GPa at Hubbard *U* = 0 and 5 eV, respectively. Moreover, the elastic constant C_{66} of YbC_6 remains unchanged at 314 GPa with Hubbard *U*, as shown in Fig. 3(d). When the independent elastic constants are obtained, the intrinsic mechanical stability of the structure at various Hubbard *U* = 0, 1, 3 and 5 eV can be verified ony the Born–Huang lattice dynamical theory. The criteria to determine the mechanical stability of cubic, tetragonal and hexagonal crystals are depicted as follows:[39]

Cubic phase (for YbC and Yb_2C_3):

$C_{11} - C_{12} > 0$, $C_{11} + 2C_{12} > 0$, $C_{44} > 0$.

Tetragonal phase (for YbC_2):

$C_{11} > |C_{12}|$, $(C_{11} + 2C_{12})C_{33} > 2C_{13}^2$, $C_{44} > 0$, $C_{66} > 0$.

Hexagonal phase (for YbC_6):

$C_{11} > |C_{12}|$, $(C_{11} + 2C_{12})C_{33} > 2C_{13}^2$, $C_{44} > 0$.

After these criteria are verified, the four ytterbium carbides with various Hubbard *U* values satisfy the criteria of mechanical stability except tetragonal YbC_2 with Hubbard *U* = 5 eV where C_{44} is negative. Specially, it is worth noticing that the NaCl-type YbC is mechanically stable, although this carbide has not been synthesized successfully.

Mechanical properties are mainly determined by the quantity including bulk modulus *B*, Young's modulus *E*, shear modulus *G*, Pugh's ratio *B*/*G* and Poisson's ratio v. Among these mechanical quantities, *B* and *G* can be obtained by Voigt–Reuss–Hill (VRH) approximation.[40-42] Under the VRH B_V, B_R, G_V, and G_R, where the subscripts V and R represent Voigt and Reuss estimations of *B* and *G*, respectively, in different crystal systems can be expressed as follows:

Cubic phase (for YbC and Yb_2C_3):[43, 44]

$B_V = B_R = (C_{11} + 2C_{12})/3$,

$Gv = (C_{11} - C_{12} + 3C_{44})/5$,

$G_R = 5(C_{11} - C_{12})C_{44}/[4C_{44}+3(C_{11} - C_{12})]$.

Tetragonal phase (for YbC_2):[45]

$B_V = (1/9)[2(C_{11} + C_{12}) + 4C_{13} + C_{33}]$,

$B_R = C^2/M$,

$G_V = (1/30)(M + 3C_{11} - 3C_{12} + 12C_{44} + 6C_{66})$,

$G_R = 15[18B_V/C^2 + 6/(C_{11} - C_{12}) + 6/C_{44} + 3/C_{66}]^{-1}$,

$M = C_{11} + C_{12} + 2C_{33} - 4C_{13}$,

$C^2 = (C_{11} + C_{12})C_{33} - 2C_{13}^2$.

Hexagonal phase (for YbC_6):[46]

$B_V = (1/9)[2(C_{11} + C_{12}) + 4C_{13} + C_{33}]$,

$B_R = C^2/M$,

$G_V = (1/30)(M + 12C_{44} + 12C_{66})$,

$G_R = (5/2)[C^2C_{44}C_{66}] / [3B_VC_{44}C_{66} + C^2(C_{44} + C_{66})]$,

$M = C_{11} + C_{12} + 2C_{33} - 4C_{13}$,

$C^2 = (C_{11} + C_{12})C_{33} - 2C_{13}^2$.

Hence, *B* and *G* are given as follows:

$B = 1/2(B_R + B_V)$ and $G = 1/2(G_R + G_V)$.

Once B and G are obtained, *E* and *υ* can be defined as follows:

$E = 9BG/(3B + G)$ and $\upsilon = (3B - 2G)/[2(3B + G)]$.

The dependence of B_V, B_R, G_V, and G_R on Hubbard *U* of YbC, Yb_2C_3, YbC_2, and YbC_6 is shown in Fig. 4. B_V, B_R, G_V, and G_R likely decrease as Hubbard *U* values increases except B_V and B_R of YbC. B_V and B_R of YbC first decreases from 103.5 GPa at *U* = 0 eV to 78.1 GPa atr *U* = 3 eV and then increases to 84.7 GPa at *U* = 5 eV in accordance with the relationship of C_{11} and C_{12} as Hubbard *U*. By contrast, Hubbard *U* slightly affect *B* and *G* of YbC_2 and YbC_6, and this result is consistent with the variation in elastic constants.

Bulk modulus *B* is measure of the resistance of a solid to volume change; shear modulus *G* represents the resistance to plastic deformation; and Young's modulus *E* denotes the resistance to uniaxial deformation. The calculated *B*, *G*, and *E* of the four ytterbium carbides with Hubbard *U* = 3 eV are listed in Table 1. Among the four ytterbium carbides, YbC_6 yields the largest *B* of 155.9 GPa, *G* of 104.8 GPa, and *E* of 256.7GPa. This result indicates that YbC_6 is stiffer than the three other ytterbium carbides. On the contrary, YbC_2 exhibits the smallest *B* of 58.2 GPa, *G* of 21.7 GPa, and *E* of 58.0 GPa. *B* of YbC_2 is only approximately one-third of that of YbC_6. Hardness and ductile will not coexist in a material. The ductile or brittle properties of materials can be related empirically to Pugh's ratio *B*/*G*. If *B*/*G* > 1.75, materials are ductile; otherwise, materials are brittle.[47] The smallest *B*/*G* of 1.49 observed in YbC_6 indicates brittleness. The largest *B*/*G* of 2.68 is detected

Table 1. Bulk modulus *B*, shear modulus *G*, Young's modulus *E*, Pugh's ratio *B*/*G*, and Poisson ration v calculated with VRH approximations of YbC, Yb_2C_3, YbC_2 and YbC_6 at Hubbard *U* = 3 eV.

	B (GPa)	*G* (GPa)	*E* (GPa)	*B*/*G*	*v*
YbC	78.1	34.2	89.6	2.28	0.309
Yb_2C_3	74.1	47.9	118.2	1.55	0.240
YbC_2	58.2	21.7	58.0	2.68	0.334
YbC_6	155.9	104.8	256.7	1.49	0.226

in YbC_2; this finding shows that YbC_2 is relatively soft and ductile. Poisson's ratio *v* generally quantifies the stability of a solid against shear deformation. For ductile materials, *v* is approximately 0.33.[48] The ductility of YbC_2 is confirmed by the calculated *v* of 0.33. Interestingly, *B* and *G* of YbC and Yb_2C_3 yield the same order of magnitude; however, *B*/*G* of YbC and Yb_2C_3 is more or less 1.75; thus, these carbides exhibit different degrees of brittleness.

3.3 Elastic Anisotropy

Anisotropic behaviors should be estimated on the basis of fundamental and technological aspects because known crystals are elastically anisotropic. Several indexes, including the percent anisotropy (A_B and A_G) and shear anisotropic factors (A_1, A_2, and A_3) have been developed to evaluate elastic anisotropy.[49] The percent anisotropy in compressibility and shear are defined as follows:

$A_B = (B_V - B_R)/(B_V + B_R)$

and

$A_G = (G_V - G_R) / (G_V + G_R)$,

respectively. For a completely isotropic system, A_B and A_G are 0, and the deviation from 0 measures the degree of elastic anisotropy. As shown in Table 2, the percent anisotropies in the shear A_G of high-symmetry cubic YbC and Yb_2C_3 systems are 0.0877 and 0.0240, respectively; whereas A_B equals 0 because of the same B_V and B_G. YbC_6 possesses the largest A_B of 0.3455 and a moderate A_G of 0.5268, whereas YbC_2 yields the largest A_G of 0.8989. This result indicates that YbC_2 displays a large anisotropy in shear. It is should be noted that A_G of the four ytterbium carbides is larger than A_B, suggesting that these carbides are slightly anisotropic in compressibility.

Shear anisotropic factors correspond to the degree of anisotropy in the bonding between atoms in different planes. A_1 of the (100) shear planes between [011] and [010] directions, A_2 of the (010) shear planes between [101] and [001] directions, and A_3 of the (001) shear planes between [110] and [010] directions are defined as follows:

$A_1 = (4C_{44}) / (C_{11}+C_{33}-2C_{13})$,

$A_2 = (4C_{55}) / (C_{22}+C_{33}-2C_{23})$,

and

$A_3 = (4C_{66}) / (C_{11}+C_{22}-2C_{12})$.

The three indexes must be identical for a completely isotropic system, and any deviation from unity corresponds to the degree of shear anisotropy. A_1, A_2, and A_3 are identical in YbC and Yb_2C_3 because of the shear isotropy of cubic structure. A_1 of YbC_2 is smaller than that of YbC_6, indicating that YbC_2 behaves more (100) shear anisotropically than YbC_6. A_3 of 0.9997 of YbC_6 demonstrates the almost isotropic property of (001) shear planes between [110] and [100] directions.

Table 2. Percent anisotropy (A_B and A_G) and shear anisotropic factors (A_1, A_2, and A_3) of YbC, Yb_2C_3, YbC_2, and YbC_6 at Hubbard *U* = 3 eV.

	A_B	A_G	A_1	A_2	A_3
YbC	0	0.0877	0.4211	0.4211	0.4211
Yb_2C_3	0	0.0240	0.6385	0.6385	0.6385
YbC_2	0.0490	0.8989	0.0095	0.0095	1.2488
YbC_6	0.3455	0.5628	0.1207	0.1207	0.9997

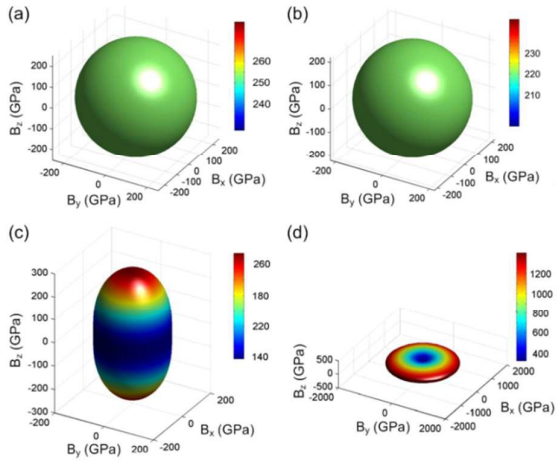

Fig. 5 Surface constructions of bulk modulus *B* of (a) YbC, (b) Yb_2C_3, (c) YbC_2, and (d) YbC_6.

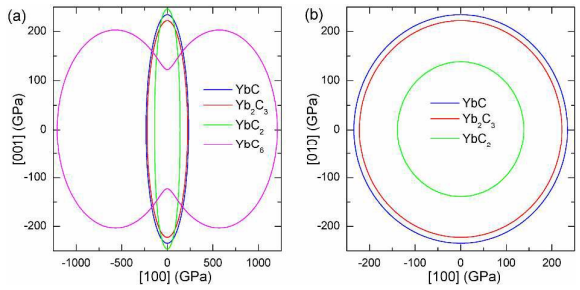

Fig. 6 Bulk modulus *B* projections on (a) (010) and (b) (001) plane of YbC, Yb_2C_3, YbC_2, and YbC_6.

A three-dimensional surface construction of *B* and *E*, along with their projections on specific planes, is plotted to describe the anisotropy of the mechanical moduli of the four ytterbium carbides. The reciprocal of *B* and *E* are defined as follows:[50]

Cubic phase (for YbC and Yb_2C_3):

$$\frac{1}{B} = s_{11} + 2s_{12}$$

$$\frac{1}{E} = s_{11} - 2(s_{11} - s_{12} - \frac{1}{2}s_{44})(l_1^2 l_2^2 + l_2^2 l_3^2 + l_1^2 l_3^2)$$

Tetragonal phase (for YbC_2):

$$\frac{1}{B} = (s_{11} + s_{12} + s_{13}) - (s_{11} + s_{12} - s_{13} - s_{33})l_3^2$$

$$\frac{1}{E} = (l_1^4 + l_2^4)s_{11} + l_3^4 s_{33} + l_1^2 l_2^2 (2s_{12} + s_{66}) + l_3^2(1 - l_3^2)(2s_{13} + s_{44})$$

Hexagonal phase (for YbC_6):

$$\frac{1}{B} = (s_{11} + s_{12} + s_{13}) - (s_{11} + s_{12} - s_{13} - s_{33})l_3^2$$

$$\frac{1}{E} = (1 - l_3^2)^2 s_{11} + l_3^4 s_{33} + l_3^2(1 - l_3^2)(2s_{13} + s_{44})$$

where l_1, l_2, and l_3 are the direction cosines in various systems, and s_{ij} is elastic compliance constant obtained using the GGA + *U* scheme with Hubbard *U* = 3 eV.

The surface constructions of *B* of YbC, Yb_2C_3, YbC_2, and YbC_6 are displayed in Fig. 5, and their *B* projections on the (010) and (001) planes are plotted in Fig. 6. The surface constructions of *B* of YbC and Yb_2C_3 exhibit a perfect sphere, indicating isotropic

characteristics because of high-symmetry cubic lattice, see Figs. 5(a) and 5(b). *B* of tetragonal YbC_2 and hexagonal YbC_6 shows strong anisotropic features. The surface construction of *B* of YbC_2 is likely an ellipsoid, see Fig. 5(c), whereas the surface of *B* of YbC_6 is similar to a disc, see Fig. 5(d). It is worth noticing that these results are in good agreement with the calculated anisotropic factors and indexes listed in Table 2. *B* projections on the (010) and (001) planes provide further details regarding anisotropic properties. The *x* axis range is five times larger than the *y* axis range to display *B* projections of the four carbides. The *B* projection on the (010) plane of YbC and Yb_2C_3, resembling an ellipse in Fig. 6(a), should be a circle. The *B* projection on the (010) plane of YbC_6 exhibits a butterfly shape, showing a strong anisotropic property. *B* projected on the (001) plane of the four ytterbium carbides is circular, which indicates an isotropic property. Due to the large *B* of YbC_6, the circular *B* on the (001) plane is noticeably larger than the three other ytterbium carbides. Fig. 6(b) illustrates only *B* of YbC, Yb_2C_3, and YbC_2 but excludes *B* of YbC_6 to show the *B* projection. The circular area of YbC is slightly larger than that of Yb_2C_3, which is consistent with *B* listed in Table 1.

The surface constructions of *E* of YbC, Yb_2C_3, YbC_2, and YbC_6 are displayed in Fig. 7, and *E* projections on the (010) and (001) planes are plotted in Fig. 8. The anisotropic property of *E* of YbC, Yb_2C_3, YbC_2, and YbC_6 is more evident than that of *B*. The surface constructions of *E* of YbC and Yb_2C_3 resemble a similar shape, see Figs. 7(a) and 7(b). *E* along the [100], [010], and [001] directions are considerably larger than *E* along other directions, indicating anisotropic features. From Fig. 8(b), it can be seen that *E* of YbC projection on the (001) plane is smaller than that of Yb_2C_3, which is consistent with that of VRH approximations listed in Table 1. The surface construction of *E* of YbC_2 is similar to a fishing float with a large value along the [001] direction, showing a strong anisotropic property. The projection of *E* of YbC_2 exhibits a rounded square, as seen in Fig. 8(b). Similar to the surface construction of *B*, the surface construction of *E* of YbC_6 is similar to a disc perpendicular to the [001] direction. Interestingly, *E* of YbC_6 in the [100] direction is obviously larger than that in the [001] direction, as shown in Fig. 8(a). The projection *E* on the (001) plane of YbC_6 is a circle but is not shown in Fig. 8(b) because of its large area.

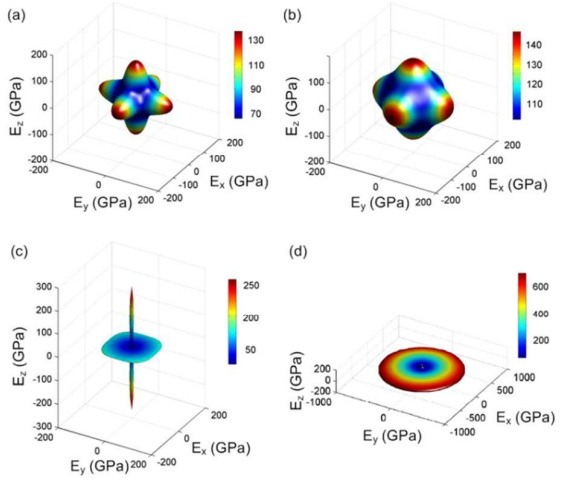

Fig. 7 Surface constructions of Young's modulus *E* of (a) YbC, (b) Yb_2C_3, (c) YbC_2, and (d) YbC_6.

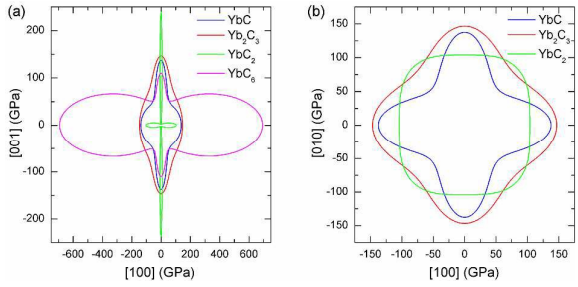

Fig. 8 Young's modulus *E* projections on (a) (010) and (b) (001) plane of YbC, Yb_2C_3, YbC_2, and YbC_6.

3.4 Anisotropy in acoustic velocities

The phase velocities of pure transverse and longitudinal modes of YbC, Yb_2C_3, YbC_2, and YbC_6 are investigated from single crystal elastic constants in accordance with the procedure developed by Brugger.[51, 52] The symmetry of crystal indictates that pure transverse and longitudinal modes can exist along specific directions: [001], [110], and [111] for a cubic crystal; [001], [110], and [100] for a tetragonal crystal; and [001] and [110] for a hexagonal crystal. In each direction, two transverse modes and one longitudinal mode are involved.[53] The calculated sound velocities of ytterbium carbides with Hubbard U = 3 eV are shown in Table 3.

In the two cubic phases, the sound velocities of Yb_2C_3 are larger than those of YbC in the [001], [110], and [111] directions. For example, the longitudinal and transverse mode velocities of Yb_2C_3 in the [001] direction are 5.6% and 34.8% larger than those of YbC. The longitudinal and transversemode velocities of the cubic system are proportional to C_{11} and C_{44}, respectively, and are inversely proportional to the density ρ which is dominated by carbon contents. C_{11} and C_{44} of Yb_2C_3 are larger than those of YbC, and the density ρ of Yb_2C_3 is smaller than that of YbC due to the relatively higher carbon contents. This leads to that the average sound velocities of Yb_2C_3 are larger than that of YbC, as shown in Fig. 9. The longitudinal and transverse vibration modes in the [001]

Table 3. Sound velocities (km/s) along different directions for YbC, Yb_2C_3, YbC_2 and YbC_6 with Hubbard U = 3 eV.

		YbC	Yb_2C_3	YbC_2	YbC_6
[001]	[001]v_l	4.019	4.245	6.101	4.563
	[110]v_{t1}	1.586	2.139	0.354	2.028
[110]	[110]v_l	3.847	4.157	4.108	11.419
	[-110]v_{t1}	2.445	2.677	2.414	7.562
	[001]v_{t2}	1.586	2.139	0.354	2.028
[111]	[111]v_l	3.397	3.817		
	[11-2]v_{t1}	2.196	2.510		
[100]	[100]v_l			3.927	
	[010]v_{t1}			2.698	
	[001]v_{t2}			0.354	

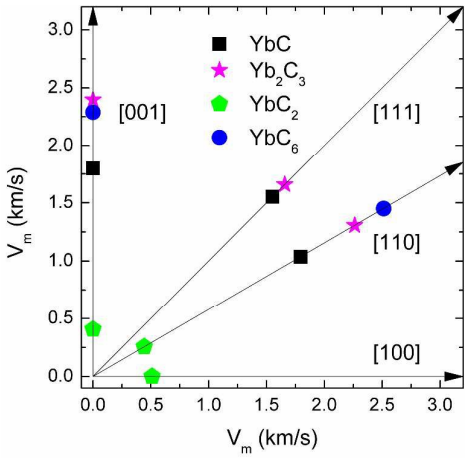

Fig. 9 Averaged sound velocities (v_m) in the [100], [001], [110] and [111] directions of YbC, Yb_2C_3, YbC_2, and YbC_6.

direction of YbC_2 are parallel and perpendicular to the C_2 dimer stretching mode. Thus, YbC_2 yields a relatively larger longitudinal mode velocity of 6.10 km/s and an extremely low transverse mode velocity of 0.35 km/s. Moreover, the significant difference between the transverse and longitudinal velocities in the [001], [100], and [110] directions results in relatively low average velocities, as shown in Fig. 9.

The longitudinal mode velocity in the [110] direction of YbC_6 is as high as 11.42 km/s, whereas two transverse mode velocities along [-110] and [001] directions are 7.562 km/s and 2.028 km/s, respectively. The sound velocity is well correlated with the structural characteristics. The longitudinal mode [110]v_l direction is the nearest C–C connecting direction in the six-membered C ring; conversely, the transverse mode [-110]v_{t1} direction is the second-nearest C–C connecting direction in the six-membered C ring. Furthermore, the large longitudinal mode velocity in the [110] direction corresponds the highest average velocity along the [110] direction among the four ytterbium carbides.

3.5 Thermodynamic properties

The calculated phonon band structures along some high-symmetry directions in Brillouin zone and the phonon projected density of states (PDOS) of YbC_2 and YbC_6 at Hubbard U = 3 eV are displayed in Fig. 10. Phonon calculations established the dynamical stability of YbC_2 and YbC_6 in view of the absence of imaginary frequencies. Additional phonon calculations of YbC and Yb_2C_3 with various Hubbard U parameters and sizes of supercells are performed. The results show that imaginary frequencies exist in their phonon band structures (data not shown here). This finding reveals that YbC and Yb_2C_3 are not thermodynamically stable, which does not coincide with the mechanical stability. This phenomenon is also found in UO_2. The *Pnma* phase of UO_2 is predicted to be mechanically stable, but is found to be thermodynamically unstable from phonon calculations.[54]

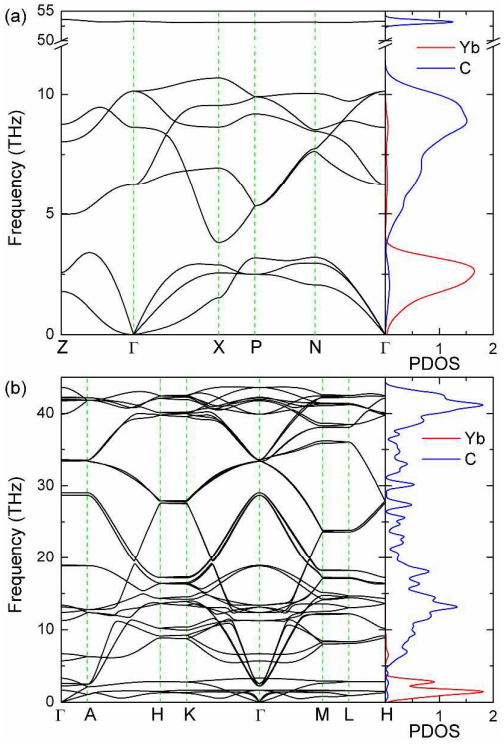

Fig. 10. Phonon band structures and PDOS of (a) YbC_2 and (b) YbC_6 with Hubbard U = 3 eV. The unit of PhDOS is states/THz/fu.

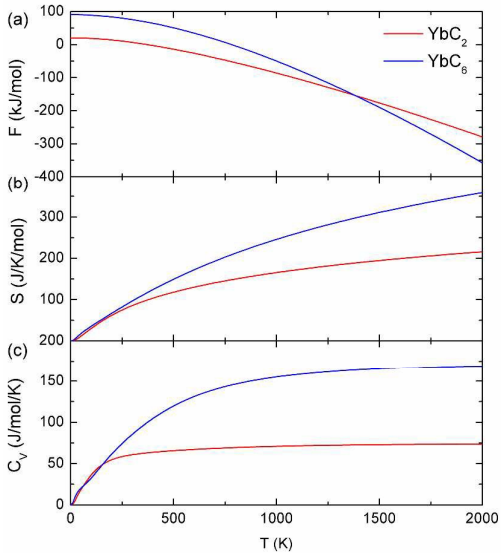

Fig. 11 Temperature dependence of (a) Helmholtz free energy (F), (b) entropy (S), and (c) heat capacity at constant volume (C_v) of YbC_2 and YbC_6 with Hubbard U = 3 eV.

The vibration frequency of the Yb atom is apparently lower than that of the C atom because the Yb atom is considerably heavier than C atom. Thus, the phonon structures of both YbC_2 and YbC_6 can be divided into two major regions. The heavy Yb atoms dominate low-frequency modes below 4 THz, whereas the light C atoms contribute significantly to high-frequency vibrations. Compared with YbC_6, the high-frequency region of

YbC_2 shifts upward and reaches approximately 53 THz. It is noteworthy that the flat regions of the phonon dispersion curves of YbC_2 as shown in Fig. 10(a), which correspond to the peaks in the phonon PDOS, indicate the localization of the states, i.e., the high-frequency stretching of C_2 units.

The temperature variations of Helmholtz free energy, entropy, and heat capacity at constant volume of YbC_2 and YbC_6 are shown in Fig. 11. It is noteworthy that the Helmholtz free energy at 0 K does not vanish because of zero-point motion. Helmholtz free energies per fu of YbC_2 and YbC_6 are 20.1 and 90.7 kJ/mol, respectively. As temperature increases, Helmholtz free energies of YbC_2 and YbC_6 decrease; however, Helmholtz free energy of YbC_6 rapidly decreases, leading to that it intersects with the Helmholtz free energy of YbC_2 at 1350 K. The entropy of YbC_6 is larger than that of YbC_2, and the difference between the entropies of these carbides increases as temperature increases. The heat capacity at constant volume of YbC_6 and YbC_2 is nearly the same below 200 K. At an intermediate temperature range, C_V is governed by atomic vibrations. Above 200 K, C_V of YbC_6 is larger than that of YbC_2. At high temperature, C_V of YbC_2 becomes constant at 75 J/mol/K, while C_V of YbC_6 reaches 170 J/mol/K.

4. Conclusions

The mechanical and thermodynamic properties of YbC, Yb_2C_3, YbC_2, and YbC_6 have been investigated with the GGA + *U* frameworks. The calculated lattice constants of YbC, Yb_2C_3, YbC_2, and YbC_6 are found to increase as Hubbard *U* values increase. The four ytterbium carbides with various Hubbard *U* values satisfy the Born−Huang lattice dynamical criteria of mechanical stability except tetragonal YbC_2 with Hubbard *U* = 5 eV. YbC_6 is stiffer than the three other ytterbium carbides, whereas YbC_2 is softest and most ductile among the four ytterbium carbides. The directional *E* and *B*, and shear anisotropic factors indicate the mechanical anisotropic properties of YbC, Yb_2C_3, YbC_2 and YbC_6. The phonon calculation reveals that YbC_2 and YbC_6 are thermodynamically stable, but NaCl-type YbC and Pu_2C_3-type Yb_2C_3 are thermodynamically unstable. These theoretical results are consistent with experimental findings.

Acknowledgements

This work was supported by the National Natural Science Foundation of China (Grants Nos. 11304269 and 11304268).

References

1 K. A. Gschneider, *Rare earth carbides*, 1991.
2 M. S. Sselhaus and G. Sselhaus, *Adv. Phys.*, 2002, **51**, 1–186.
3 S. Ma, K. Bao, Q. Tao, X. Huang, P. Zhu and T. Cui, *RSC Advances*, 2014, **4**, 63544–63548.
4 D. D. Kumar, N. Kumar, S. Kalaiselvam, R. Radhika, S. Dash, A. K. Tyagi and R. Jayavel, *RSC Advances*, 2015, **5**, 81790–81801.
5 L. Brewer and O. Krikorian, *J. Electrochem. Soc.*, 1955, **103**, 701–703.
6 M. E. Makrini, D. Guérard, P. Lagrange and A. Hérold, *Physica B+C*, 1980, **99**, 481–485.
7 M. E. Makrini, D. Guérard, P. Lagrange and A. Hérold, *Carbon*, 1980, **18**, 203–209.
8 M. H. Upton, T. R. Forrest, A. C. Walters, C. A. Howard, M. Ellerby, A. H. Said and D. F. McMorrow, *Phys. Rev. B*, 2010, **82**, 134515.
9 V. Babizhetskyy, O. Jepsen, R. K. Kremer, A. Simon, B. Ouladdiaf and A. Stolovits, *J. Phys.: Condens. Matter*, 2014, **26**, 025701.
10 C. Zhang, S. T. John, T. Kaori and H. Q. Lin, *EPL-Europhys. Lett.*, 2012, **100**, 67003.
11 Y. L. Li, W. Luo, Z. Zeng, H. Q. Lin, H. k. Mao and R. Ahuja, *Proc. Natl. Acad. Sci. U. S. A.*, 2013, **110**, 9289–9294.
12 Y. L. Li, S. N. Wang, A. R. Oganov, H. Gou, J. S. Smith and T. A. Strobel, *Proc. Natl. Acad. Sci. U. S. A.*, 2015, **6**, 6974.
13 Y. L. Li, W. Luo, X. J. Chen, Z. Zeng, H. Q. Lin and R. Ahuja, *Sci. Rep.*, 2013, **3**, 3331.
14 F. H. Spedding, K. Gschneidner and A. H. Daane, *J. Am. Chem. Soc.*, 1958, **80**, 4499–4503.
15 J. M. Haschke and H. A. Eick, *J. Am. Chem. Soc.*, 1970, **92**, 1526–1530.
16 K. A. Gschneidner and F. W. Calderwood, *Bull. Alloy Phase Diagrams*, 1986, **7**, 568–570.
17 M. Atoji and R. H. Flowers, *J. Chem. Phys.*, 1970, **52**, 6430–6431.
18 T. E. Weller, M. Ellerby, S. S. Saxena, R. P. Smith and N. T. Skipper, *Nat. Phys.*, 2005, **1**, 39–41.
19 G. Csányi, P. B. Littlewood, A. H. Nevidomskyy, C. J. Pickard and B. D. Simons, *Nat. Phys.*, 2005, **10**, 1038.
20 I. I. Mazin, *Phys. Rev. Lett.*, 2005, **95**, 227001.
21 M. Calandra and F. Mauri, *Phys. Rev. Lett.*, 2005, **95**, 237002.
22 V. I. Anisimov, J. Zaanen and O. K. Andersen, *Phys. Rev. B*, 1991, **44**, 943–954.
23 S. L. Dudarev, G. A. Botton, S. Y. Savrasov, C. J. Humphreys and A. P. Sutton, *Phys. Rev. B*, 1998, **57**, 1505–1509.
24 A. I. Liechtenstein, V. I. Anisimov and J. Zaanen, *Phys. Rev. B*, 1995, **52**, R5467–R5470.
25 I. I. Mazin and S. L. Molodtsov, *Phys. Rev. B*, 2005, **72**, 172504.
26 M. Neupane, S. Y. Xu, N. Alidoust, G. Bian, D. J. Kim, C. Liu, I. Belopolski, T. R. Chang, H. T. Jeng and T. Durakiewicz, *Phys. Rev. Lett.*, 2015, **114**, 016403.
27 G. Kresse and J. Furthmüler, *Phys. Rev. B*, 1996, **54**, 11169–11186.
28 G. Kresse and D. Joubert, *Phys. Rev. B*, 1999, **59**, 1758–1775.
29 H. J. Monkhorst and J. D. Pack, *Phys. Rev. B*, 1976, **13**, 5188–5192.
30 J. P. Perdew, K. Burke and M. Ernzerhof, *Phys. Rev. Lett.*, 1996, **77**, 3865–3868.
31 K. Parlinski, Z. Q. Li and Y. Kawazoe, *Phys. Rev. Lett.*, 1997, **78**, 4063–4066.
32 A. Togo, F. Oba and I. Tanaka, *Phys. Rev. B*, 2008, **78**, 134106.
33 A. Togo, L. Chaput, I. Tanaka and G. Hug, *Phys. Rev. B*, 2010, **81**, 174301.
34 T. Mochiku, T. Nakane, H. Kito, H. Takeya, S. Harjo, T. Ishigaki, T. Kamiyama, T. Wada and K. Hirata, *Physica C*, 2005, **426–431**, 421–425.
35 R. K. Kremer, J. S. Kim, W. H. Xie, V. Babizhetskyy, O. Jepsen, A. Simon, K. S. Ahn, B. Raquet, H. Rakoto and J. M. Broto, *Phys. Rev. B*, 2007, **76**, 014516.
36 D. W. Jones, I. J. McColm, R. Steadman and J. Yerkess, *J. Solid State Chem.*, 1984, **53**, 376–381.
37 M. Atoji, *J. Chem. Phys.*, 1961, **35**, 1950–1960.
38 C. M. Fang, J. Bauer, J. Y. Saillard and J. F. Halet, *Verlag der Zeitschrift für Naturforschung*, 2007, **38**, 971–976.
39 F. Mouhat and F. X. Coudert, *Phys. Rev. B*, 2014, **90**, 224104.
40 W. Voigt, *Lehrburch der Kristallphysik*, Teubner, Leipzig, 1928.

41 A. Reuss, *Z. Angew. Math. Mech.*, 1929, **9**, 49.
42 R. Hill, *Proc. Phys. Soc. A*, 1952, **65**, 349–354.
43 J. Feng, B. Xiao, R. Zhou, W. Pan and D. R. Clarke, *Acta Mater.*, 2012, **60**, 3380–3392.
44 X. Gao, Y. Jiang, R. Zhou and J. Feng, *J. Alloy. Compd.*, 2014, **587**, 819–826.
45 J. P. Watt, *J. Appl. Phys.*, 1986, **60**, 3120–3124.
46 J. P. Watt and L. Peselnick, *J. Appl. Phys.*, 1980, **51**, 1525–1531.
47 S. F. Pough, *Philo. Mag.*, 1954, **45**, 823–843.
48 J. Haines, A. Jm Léger and G. Bocquillon, *Annu. Rev. Mater. Res.*, 2001, **31**, 1–23.
49 P. Ravindran, L. Fast, P. A. Korzhavyi and B. Johansson, *J. Appl. Phys.*, 1998, **84**, 4891–4904.
50 J. F. Nye, *Physical properties of crystals*, Oxford University Press, Oxford, UK, 1985.
51 K. Brugger, *J. Appl. Phys.*, 1965, **36**, 768–773.
52 K. Brugger, *J. Appl. Phys.*, 1965, **36**, 759–768.
53 J. Feng, B. Xiao, Z. C. Huang, J. C. Chen, C. L. Wan, Z. X. Qu, R. Zhou and W. Pan, *Acta Mater.*, 2010, **72**, 1742–1760.
54 B. T. Wang, P. Zhang, R. Lizárraga, I. Di Marco and O. Eriksson, *Phys. Rev. B*, 2013, **88**, 1047.

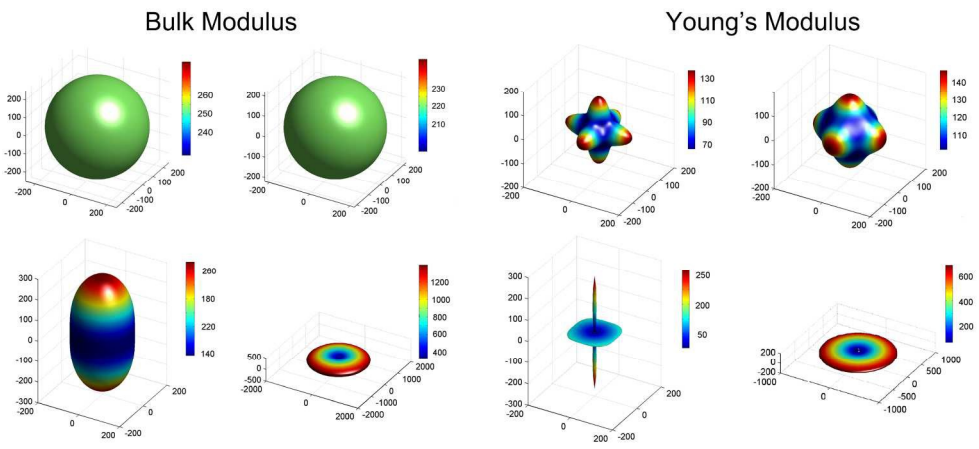

194x86mm (300 x 300 DPI)